An emulation-based approach for interrogating reactive transport models

1   **Authors:** Angus Fotherby[1*], Harold J. Bradbury[1], Jennifer L. Druhan[2], Alexandra V. Turchyn[1]

2   1: Department of Earth Sciences, University of Cambridge, Cambridge, UK

3   2: Department of Geology, University of Illinois at Urbana Champaign, Urbana, IL

4   *corresponding author: af606@cam.ac.uk

5   **Keywords:** Environmental remediation, Reactive transport, Machine learning, Sensitivity analysis

6   **Abstract**

7   We present a new approach to understand the interactions among different chemical and biological

8   processes modelled in environmental reactive transport models (RTMs) and explore how the

9   parameterisation of these processes influences the results of multi-component RTMs. We utilize a

10 previously published RTM consisting of 20 primary species, 20 secondary complexes, 17 mineral

11 reactions and 2 biologically-mediated reactions which describes bio-stimulation using sediment from

12 a contaminated aquifer. We choose a subset of the input parameters to vary over a range of values.

13 The result is the construction of a new dataset that describes the model behaviour over a range of

14 environmental conditions. Using this dataset to train a statistical model creates an emulator of the

15 underlying RTM. This is a condensed representation of the original RTM that facilitates rapid

16 exploration of a broad range of environmental conditions and sensitivities. As an illustration of this

17 approach, we use the emulator to explore how varying the boundary conditions in the RTM

18 describing the aquifer impacts the rates and volumes of mineral precipitation. A key result of this

19   work is the recognition of an unanticipated dependency of pyrite precipitation on pCO_2 in the

20   injection fluid due to the stoichiometry of the microbially-mediated sulphate reduction reaction. This

21   complex relationship was made apparent by the emulator, while the underlying RTM was not

22   specifically constructed to create such a feedback. We argue that this emulation approach to

23   sensitivity analysis for RTMs may be useful in discovering such new coupled sensitives in

24   geochemical systems and for designing experiments to optimise environmental remediation. Finally,

25   we demonstrate that this approach can maximise specific mineral precipitation or dissolution

26   reactions by using the emulator to find local maxima, which can be widely applied in environmental

27   systems.

28   **Synopsis**

29   This study explores key factors regulating mineralization reactions in near surface environments

30   revealed by a machine learning approach to reactive transport modelling.

31   **1   Introduction**

32   Reactive transport modelling has been extensively applied across a wide variety of environmental

33   systems, providing a powerful means of quantifying, and even predicting, processes across Earth's

34   (near) surface environments (Richter and DePaolo, 1987; Bain et al., 2000; Johnson et al., 2004; van

35   Breukelen et al., 2004; Gaus et al., 2005; Torres et al., 2015; Li et al., 2017; Arora et al., 2020;

36   Molins and Knabner, 2020; Rolle and Borgne, 2020; Druhan et al., 2020; Cama et al., 2020).

37   Reactive transport models (RTMs) are constructed by combining multiple physical, chemical, and

38   biological processes to simulate the behaviour of environmental systems. As applications and

39   software have concurrently expanded (Steefel et al., 2015; Li et al. 2017; Maher & Mayer, 2019;

40   Druhan & Tournassatt, 2019), it is becoming increasingly common to explicitly calculate the rates of

41   production and consumption for a variety of coexisting chemical species, as well as their equilibria

42   with mineral phases, and their transport as they evolve in time and space. This type of multi-phase,

43   multi-component RTM is a type of forward modelling where the results of the simulation emerge

44   from a complex suite of interacting pathways, and hence the causes of observed behaviour are not

45   always obvious.

46   RTMs are often designed to describe the behaviour of specific field sites and systems. Due to their

47   process-based nature, designing RTMs requires selection of a suite of chemical reactions and

48   transport mechanisms which are thought to dominate the geochemistry of the system over the scales

49   of interest. However, the parameterisation of various selected processes is often not unique and can

50   impact system behaviour (Williams et al., 2011; Martinez et al., 2014; Seigneur et al., 2021; Steefel

51   et al., 2005a). To assess the impact of the choice of parameterisation and the values chosen for

52   different parameters on model predictions, sensitivity analyses are generally performed (Malaguerra

53   et al., 2013; Gatel et al., 2019). However, as RTMs become increasingly sophisticated, they

54   incorporate disparate processes that can interact with each other in complex ways (Dwivedi et al.,

55   2018; Hubbard et al., 2018, 2019; Maavara et al., 2021a, b; Dwivedi et al., 2017).

56   The sensitivity analysis of an RTM in application to a specific environmental system can elucidate

57   the relative importance of specific interactions; for example, testing the solubility of mineral phases

58   relative to changes in the solution chemistry. However, results might emerge that were not

59   anticipated. These results might represent a real, but unexpected, interaction in which case the

60   sensitivity analysis has yielded new insight into the system being modelled. Equally, the result might

61   represent an incorrect interaction between two different processes that are known to act

62   independently of each other, in which case the RTM can be improved. Unfortunately, due to the

63   computational expense of many modern multi-component RTMs (e.g. Abd and Abushaikha, 2021;

64   Seigneur et al., 2021; Gharasoo et al., 2022), it is normally impractical to perform sensitivity analyses

65   in more than a few dimensions and it is up to the investigator to use their knowledge of the system to

66   choose which sensitivity analyses are necessary to explore (Steefel et al., 2005b). Ideally, we would

67   be able to systematically perform sensitivity analyses over many model parameters, considering how

68   model outputs vary as a function of multiple input parameters simultaneously (i.e. in a multivariate

69   way), while also lightening the computational burden that commonly occurs when using inverse

70   modelling approaches implemented by codes like PEST and iTOUGH2 (Doherty, 2004; Finsterle et

71   al., 2017). Such a capacity could direct future laboratory-based investigations to test whether these

72   model results are real-world phenomena, ultimately offering improved parameterisation of critical

73   components within the reaction network.

74   Here, we demonstrate an approach to explore a wide variety of potential model parameters, by

75   adapting an emulation method similar to that previously applied in physics-based animation

76   (Grzeszczuk et al., 1998) to complex multi-physics simulators (Lu et al., 2021; Bianchi et al., 2016)

77   and climate models (Beucler et al., 2019; Krasnopolsky et al., 2005; Castruccio et al., 2014;

78   Kashinath et al., 2021) as well as applied to emulating fluid flow through Dolomite using a neural

79   network (Li et al., 2022). In this emulation approach, the underlying physical system is approximated

80   by a statistical model (the emulator) which can be evaluated more quickly than a conventional

81   forward model. How this emulator is constructed varies by implementation and may encode

82   assumptions about the underlying system to be modelled (e.g. conservation of energy (Beucler et al.,

83   2019)). In our implementation the emulator is built by training a Gradient Boosted Trees (GBT)

84   regressor (Chen and He, 2015) on a synthetic dataset generated from the original RTM. By training

85   such a GBT model on the synthetic dataset generated by the original RTM, we create an emulator of

86   the original system. This emulation approach is general and can be applied to a wide range of RTMs,

87   using "off the shelf" statistical libraries, requiring no special construction of the statistical model

88   beyond the choice of some training parameters. This approach can identify the critical processes and

89   parameters within RTMs and address the requirement for comprehensive, multivariate sensitivity

90   analyses.

91   We first present a tool that automates creation of synthetic datasets: a Python wrapper for the RTM

92   software CrunchTope (Druhan et al., 2013; Steefel et al., 2015), which we have named Omphalos.

93   Omphalos edits and runs CrunchTope input files in an automated fashion, systematically changing

94   model parameters according to user specification. It then records the output data, along with the

95   corresponding model input parameters for later analysis. We then apply a machine learning method

96   (Gradient Boosted Trees) to these recorded inputs and outputs to create a predicative model that can

97   reproduce RTM outputs based on the input variables, which we term a Reactivate Transport

98   Emulator (RTE).

99   We envision that such Reactive Transport Emulators could be used to direct new experimental

100   investigation to identify and corroborate predicted dependencies; providing much-needed

101   multivariate analysis of RTMs and helping to identify effects that can, in the future, be considered

102   explicitly when developing new RTMs. In pursuit of this goal, we demonstrate our emulator

103   approach in application to an RTM built for biostimulation of a contaminated aquifer. We also show

104   an additional application of this approach to efficiently predict the condition which maximises an

105   RTM-predicted time-integrated rate over the set of chosen parameters. We also present, in the

106   Supporting Information, another example in application to a deep-sea sediment column.

107   **2   Description of the Case Study**

108   **2.1   Old Rifle Site, Colorado**

109   The Old Rifle site is located near Rifle, Colorado, USA. The location historically hosted a vanadium

110   and uranium ore processing facility, and the groundwater at the site remains high in aqueous

111   uranium. Oxidised uranium (U(VI)) is fluid-mobile and highly toxic, while reduced uranium (U(IV))

112   is much less soluble and forms stable precipitates such as uraninite (UO_2) (Anderson et al., 2003; Wu

113   et al., 2006; Dullies et al., 2010; Williams et al., 2011; Long et al., 2015). Thus, uranium reduction

114   has been suggested as a means for remediating uranium contamination in groundwater. It has been

115   shown that iron sulfide minerals ($FeS_{2(s)}$) aid the reduction of soluble U(VI) to insoluble U(IV)

116   precipitates even after active remediation has ceased (Komlos et al., 2008; Moon et al., 2010; Bargar

117   et al., 2013; Long et al., 2015; Bone et al., 2017).

118   The RTM published for Old Rifle, upon which the RTE is based, was originally created as a

119   comprehensive model of microbial sulfate reduction and sulfide precipitation in Old Rifle sediment

120   during stimulation of microbial activity by amendment with $C_2H_3O_2^-$ (Druhan et al., 2014) (for a

121   schematic illustration of this RTM, see Fig. S2). In this context, we choose to vary the influent

122   boundary condition chemistry, representing changes to the chemical composition of the artificial

123   groundwater injectate. The original experiment was designed to model microbial sulfate and iron

124   reduction in the sediment; therefore, we use net amorphous iron (II) sulfide ($FeS_{(am)}$), and pyrite

125   ($FeS_{2(s)}$) precipitation (both hereafter referred to simply as 'pyrite') as an observable that will record

126   the sensitivities of the model predictions to changes in the injection fluid. We also demonstrate the

127   utility of the emulator in predicting the chemical composition of the injection fluid that will

128   maximise the volume of pyrite precipitated in the sediments when amended with a labile organic

129   carbon source via injection wells.

130   **3   Methodology**

131   **3.1   General Strategy**

132   To explore the dependence of the RTM on the chosen environmental variables, we begin with a

133   Monte Carlo approach; we draw random values for each parameter and record the model output

134   under that randomised condition. We then fit a model to this Monte-Carlo-generated dataset using a

135   GBT regressor. This fitting results in a model (our emulator—RTE) that reproduces the complex

136   interdependencies of chemical species that are encoded in the original, underlying, RTM. This

137   emulator can be interrogated to examine the dependence of the RTM outputs on the originally chosen

138   environmental variables in an efficient, multivariate way. This new way of performing sensitivity

139   analyses has the potential to give insight into trends and relationships that would not be apparent

140   otherwise and ultimately allows us to investigate the sensitivity of the model outputs with respect to

141   the RTM's original parameterisation. First, we will describe how we use the Monte Carlo approach

142   to generate data and then how we fit a model to this data. The overall workflow is shown in Figure 1.

143
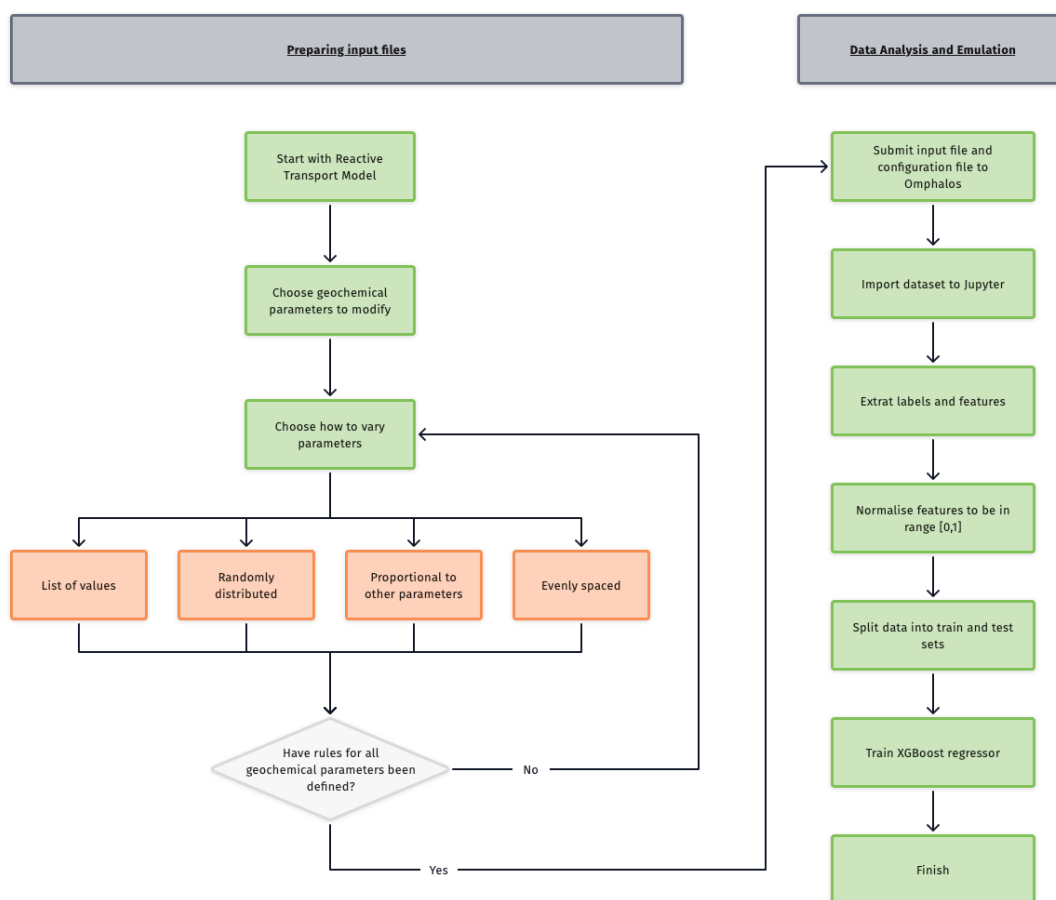
Figure 1: Flowchart describing the overall reactive transport emulation workflow developed in this study. It is divided into two key sections: preparation of the input reactive transport model for submission to Omphalos, and the analysis and emulation of the resultant data.

3.2 Generating Data

We use the open-source software CrunchTope as the reactive transport framework for the models in this study. To generate the synthetic datasets necessary for our approach and given the time-consuming nature of generating a single point (requiring a complete run of the RTM, along with modified boundary conditions), we developed a software package in Python to automate this process. This software package can manage the automatic generation and submission of unique input files to

153   CrunchTope, as well as recording the output of each run, storing it in a manageable data structure for

154   future use. Use of the software package is straight-forward, requiring the configuration of a single file

155   listing which species/parameters are to be varied, and how they should be varied.

156   We have named this software package Omphalos (available for download—Sect. 6.1). Omphalos can

157   be run on clusters using Simple Linux Utility for Resource Management (Yoo et al., 2003) to execute

158   input files in parallel, which considerably reduces the time required to generate large datasets.

159   Omphalos works by taking random values which are drawn from uniform distributions (other

160   statistical distributions are possible) of the chosen variables, sampling the space evenly. This

161   provides a complete dataset for training the emulator.

162   While the underlying principle of training emulators on synthetic data can be applied to any reactive

163   transport code, currently the software used to implement the approach is only compatible with

164   CrunchTope, because the input file reading and writing must be in a specific format. The approach is

165   readily generalized, however, and the methodology could be applied to any RTM software (e.g.

166   Geochemist's Workbench, ToughReact), provided that the string input/output code is adapted for

167   compatibility. To use other RTMs with Omphalos, two key factors need to be addressed:

168   compatibility with Omphalos, and the computational expense of a single RTM run.

169   **3.3   Application to Contaminated Aquifer Case Study**

170   We begin by applying the emulation methodology to our case study. To create the dataset for training

171   the emulator, we collected the results of 10,927 unique CrunchTope simulations based on the original

172   RTM describing Old Rifle using Omphalos, drawing random concentrations for each species in the

173   boundary condition. Of these 10,927 runs, 9416 provide useable data because some runs fail to

174   converge within the specified timeframe, or the geochemical condition generated cannot be charge

175   balanced by CrunchTope. The concentrations for NH_4^+, SO_4^{2-}, Ca^{2+}, and $C_2H_3O_2^-$ are varied between

176   0–30 mM. The pCO2 is varied between 0–10 bar. We acknowledge that these ranges of

177   concentrations are somewhat higher than those that occur in natural systems, but we extend the range

178   to observe RTM behaviours at limiting concentrations. Related to this, it is possible for the dominant

179   reaction mechanism in a system to change under differing conditions (e.g. the change in calcite

180   dissolution mechanism as a function of pH (Dolgaleva et al., 2005)) and any such behaviour should

181   be explicitly encoded into the RTM, otherwise the emulator may give invalid predictions under

182   conditions that are far from the original model run. We have assumed in this study that the

183   mechanisms governing the precipitation of pyrite do not change under very low or very high

184   concentrations of these species.

185   The injection fluid was constrained at pH 7.2. This constraint, in conjunction with the concentration

186   of various species iterated in Omphalos, speciates according to CrunchTope's internal speciation

187   calculation. Therefore, for example, although the total amount of SO_4^{2-} in the injection will be iterated

188   in, and dictated by, Omphalos, the amount that speciates into other aqueous complexes (i.e.

189   secondary species) like HSO_4^- or $H_2SO_{4(aq)}$ is controlled by CrunchTope. For the sake of simplicity,

190   we will report the input concentration, not the concentration after speciation.

191   The RTM describing Old Rifle has 100 grid cells with a size of 1 cm. Each run of the RTM took

192   approximately 90 seconds, so the total time to generate the dataset was roughly four hours when run

193   on a remote machine with 200 CPUs. The number of runs was chosen as a balance between what was

194   computationally tractable and the ability of the emulator to achieve a good fit. We have intentionally

195   chosen to vary some chemical species in the influent boundary condition that do not play an obvious

196   role in the mineral precipitation process we are particularly interested in, namely, the precipitation of

197   pyrite in Old Rifle sediments (e.g., NH_4^+ or Ca^{2+}, respectively). We did this to see if we can use the

198   emulator to detect behaviour in the RTM beyond what we might initially hypothesise.

199 **3.4 Fitting the emulator**

200 We implement the GBT regressor using XGBoost (Chen and He, 2015) in Python. The code for

201 fitting the models is available in the Supporting Information. For a precis on GBT models, see the

202 supplement Sect. S1.2.

203 **3.4.1 Data Strategy**

204 Data generated by Omphalos was imported into a Jupyter notebook environment from the .pkl output

205 file. There are 9416 different input file runs in this data file. The relevant data was indexed out of the

206 data structure; in our case this meant the concentrations of NH_4^+, SO_4^{2-}, Ca^{2+}, and $C_2H_3O_2^-$ in the

207 boundary condition, as well as value of pCO_2. This results in a 5x9416 array of floating-point

208 numbers for the features. Each feature was then normalised to be in the range 0 to 1 for training. For

209 example, values of SO_4^{2-} concentration in the simulations were drawn randomly between 0 and 30

210 mM, so all SO_4^{2-} concentrations were divided through by 30 to have values in the range 0–1. We did

211 this to improve the training performance of the GBT model over different datasets (i.e. so that the

212 same GBT model can be applied to both the Old Rifle case study, and our supplementary case study

213 of ODP Site 1086 (see Supplement, Sect. 3).

214 Similarly, the relevant data was also extracted from the data file: for each cell in the gridded RTM,

215 we calculated the net pyrite precipitation over the course of the simulation, and then summed this

216 value over the column to get the net pyrite precipitated across the domain. This results in a 1x9416

217 array of floating-point labels to be predicted from the feature array. We scale this feature array by a

218 factor of 1×10^4 to avoid issues with small floating-point numbers in XGBoost.

219 We prepared these data for training the GBT regressor with a hold-out strategy using the

220 scikitlearn.train_test_split method, keeping 10% of the dataset back for validating the model. Data

221 was split randomly within the dataset. This means that 8474 randomly selected data points were used

222   to train the model and 942 randomly selected data points were used to test it by using the model to

223   predict a value based on the held back data and comparing the prediction to the true value.

3.4.2 Training Strategy

225   We use the test set of data points generated by Omphalos to train an XGBoost regressor using

226   squared error as the loss function to predict the amount of pyrite precipitated in the column as a

227   function of varied species concentrations in the boundary condition. Squared log loss, and pseudo-

228   Huber error we also tried but squared loss performed best overall. Training curves showing the

229   testing and training loss as training progressions are given the supplement, Fig. S4.

230   Hyperparameter choices for the model are explained and given in the supplement, Sect. S1.3, Table

231   S1. The choice of hyperparameters is the same for each emulator model, and we are able to achieve

232   high quality fits using the default XGBoost regularisations, only changing a few settings relating to

233   tree growth policy. While it is a known problem in machine learning that the choice of optimal

234   hyperparameter is dependent on the data being modelled (Claesen and De Moor, 2015), it appears

235   that in the context of these RTEs, the hyperparameters chosen give a good fit for both Old Rifle and

236   our supplementary case study of ODP Site 1086: datasets describing very different natural

237   environments, with different length and time scales. This makes the workflow applicable across a

238   wide variety of reactive transport modelling domains.

239   It is possible that with more complex hyperparameter tuning, better emulator fits may be achieved,

240   but for the purposes outline in this paper, we suggest that this automated optimisation of a subset of

241   the available hyperparameters is sufficient, and represents a balance between emulator fit,

242   generalisability across differing RTMs, and time spent by the user.

4   Results and discussion

4.1   Application to the Old Rifle Site

245   The synthetic data generated using Omphalos to interrogate the underlying RTM are shown in Fig. 2,

246   colour mapped by the pCO_2 with which the injectate solution is in equilibrium. The colour mapping

247   helps visualise how variability in the precipitated volume of pyrite over the 43-day RTM simulation

248   might be considered in conjunction with other model parameters. Ultimately, pyrite forms because

249   aqueous hydrogen sulfide, produced through microbial sulfate reduction, reacts with reduced ferrous

250   iron (Fe(II)) to form pyrite. Thus, we aim to explore the interdependencies between the mechanisms

251   driving microbial sulfate reduction and the subsequent precipitation of pyrite, as they emerge due to

252   variations in injectate chemical composition.
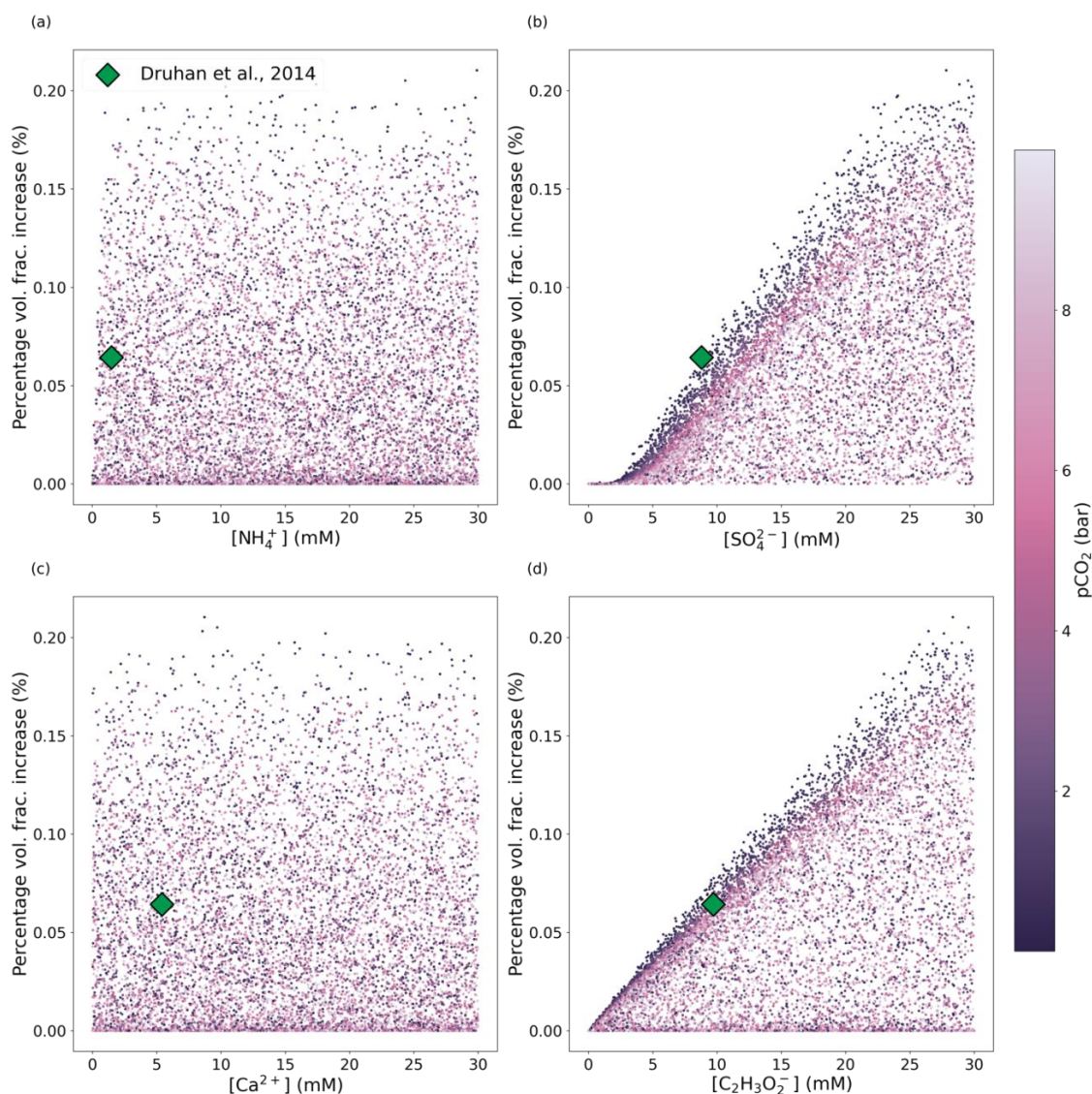
Figure 2: Scatter plots of chemical concentrations in the fluid injectate (influent boundary condition) for an RTM adapted to Old Rifle sediments colour-mapped by the pCO₂ with which the inlet boundary condition is in equilibrium. The dataset comprises 9416 points generated by drawing concentrations for all five species independently from uniform random distributions, with the corresponding net increase in pyrite volume fraction precipitated (y-axis) calculated by running the Old Rifle RTM designed by Druhan et al. (2014) with the randomised influent

260   **boundary condition. The green diamond indicates the net pyrite volume fraction generated**

261   **from the original boundary condition used in Druhan et al. (2014).**

262   We then train the emulator on this synthetic dataset. Fitting a GBT regressor to the data in Fig. 2

263   means Fig. 3 can be generated by the emulator. This figure shows how the emulator predicts the

264   change in pyrite volume fraction as the concentration of each of the species in the injection fluid is

265   varied (other species in the RTM not defined as variables in this study are held constant at values

266   reported by Druhan et al. (2014)). The convergence of the emulator is shown in Fig. S3. We stress

267   that the RTM results shown in Fig. 3 are not part of the training dataset, and that the emulator has not

268   been exposed to these exact values. This demonstrates the capability of the emulator to reproduce the

269   underlying RTM itself. For example, Fig. 2A suggests visually that the concentration of NH_4^+ in the

270   system is uncorrelated with net pyrite precipitation at the Old Rifle Site. Fig. 3A confirms this lack of

271   dependence on NH_4^+.

272   In contrast to the minimal impact that changing NH_4^+ concentration has on pyrite precipitation,

273     $C_2H_3O_2^-$ and SO_4^{2-} concentrations correlate strongly with net pyrite precipitation. This is as expected

274   in a system where $C_2H_3O_2^-$, which is the electron donor for microbial sulfate reduction, enables

275   sulfate to be reduced to sulfide and thus drive pyrite precipitation in the presence of Fe(II).

276   Approximately 20 days after $C_2H_3O_2^-$ amendment, microbial sulfate reduction takes over from

277   dissimilatory iron reduction as the dominant process consuming $C_2H_3O_2^-$. As microbial sulfate

278   reduction requires eight-times the number of electrons per mole of SO_4^{2-} reduced than dissimilatory

279   iron reduction requires (per mole of iron reduced), the electron donor ($C_2H_3O_2^-$) begins to be rapidly

280   consumed, whereas during dissimilatory iron reduction it was effectively in excess. As a result of this

281   new scarcity of $C_2H_3O_2^-$, the rate of dissimilatory iron reduction drops and so does the concentration

282   of Fe(II). However, dissimilatory iron reduction is still active in the column, releasing a small—but

283   non-zero—flux of aqueous Fe(II) that allows for continued pyrite precipitation. The emulator

284   interprets this as Fe(II) being 'always' available in this system, and thus predicts that pyrite

285   precipitation can scale linearly with SO_4^{2-} and $C_2H_3O_2^-$, as shown in Fig, 4A. The sediment itself

286   would need to contain abundant ferrihydrite, goethite, or another bioavailable ferri(hydr)oxide for

287   this reduction to continue indefinitely; this may not be the case. This highlights the need for the range

288   of parameters sampled when training the emulator to be sufficiently wide to capture all the RTM

289   behaviour, otherwise it may extrapolate and "learn" incorrect assumptions about the system: in this

290   case that bioavailable iron never limits dissimilatory iron reduction. One solution would be to expand

291   the range over which concentrations are drawn to reach the limit where iron-bearing mineral volume

292   fraction becomes a limiting factor so that the model can learn what happens when this occurs.

293
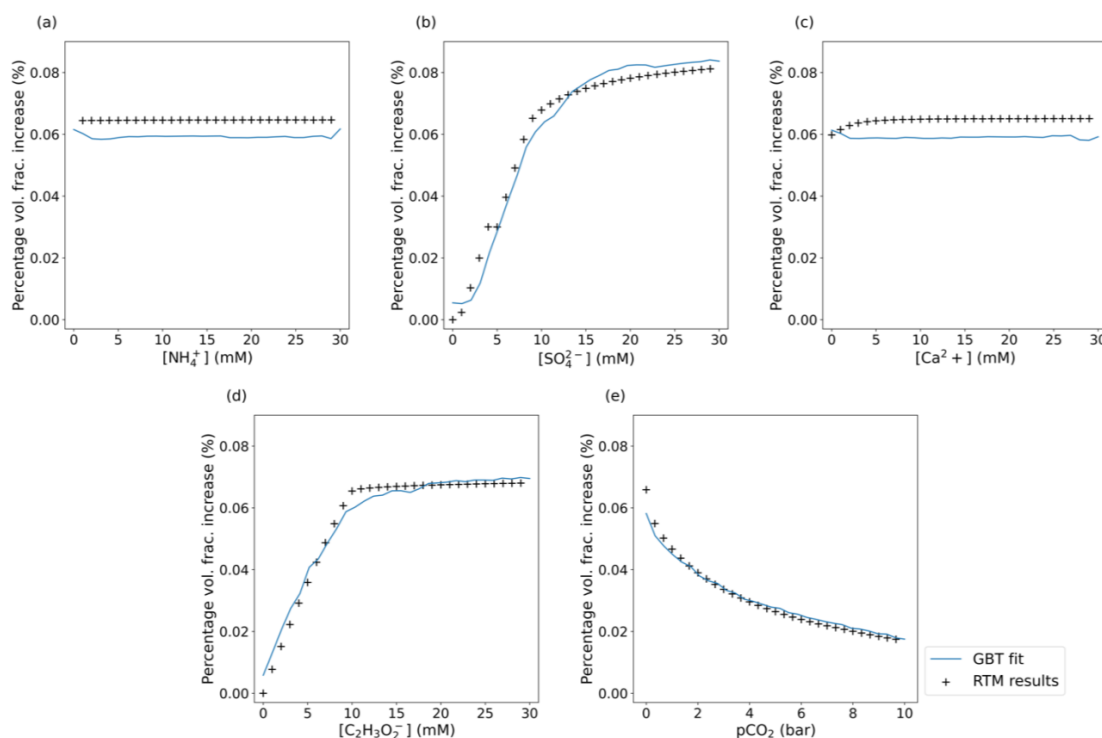
Figure 3: Plots of the GBT model fit (blue line) plotted over the results from the underlying

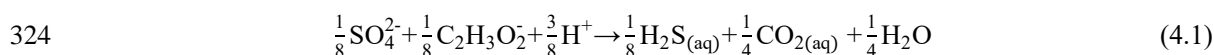**RTM (black + symbols) when interrogated with the same input parameters (which are taken as**

296   **ground truth). Each plot shows the net volume fraction due to pyrite precipitation as a**

297   **percentage of the initial volume fraction of the sediment as each parameter is varied while all**

298   **other parameters are held at the values used in the original experiment by Druhan et al. (2014).**

299   **The emulator (blue line) captures the overall trends in the data. The lack of smoothness in the**

300   **emulator predications arises from the inability to encode this as a condition in XGBoost and**

301   **the discreet nature of the decision tree algorithm.**

302   We also note that our emulator suggests that increasing pCO_2 leads to decreased pyrite precipitation

303   (Figure 4E), a relationship that may not have been apparent in a single run of the RTM. Three-

304   dimensional visualisation of the data confirms that the pyrite-volume-fraction-change varies as a

305   function of pCO_2 net pyrite precipitated decreasing as pCO_2 increases (Fig. 4B and Fig. 4C). This

306   three-dimensional visualisation allows us to see that the gradient of the pyrite-volume-fraction-

307   change with respect to SO_4^{2-} and $C_2H_3O_2^-$ is itself a function of pCO_2 and flattens as pCO_2 increases.

308   To understand why the gradient changes, we must first understand why pCO_2 affects the amount of

309   pyrite precipitated in the first place.

310   Sediment samples from Old Rifle are initially poised for dissimilatory iron reduction and there is a

311   sizeable community of iron-reducing bacteria naturally present in the system. The background

312   sulfate-reducing microbial community is initially relatively small and thus, for microbial sulfate

313   reduction to proceed at significant rates, the mass of sulfate-reducing bacteria must first increase. In

314   the original experiment by Druhan et al. (2014), the sulfate-reducing biomass begins reaching a size

315   where it can start consuming large quantities of $C_2H_3O_2^-$ around day 20 of the experiment. This

316   biomass growth is modelled in CrunchTope using a Monod-biomass rate law (Jin and Bethke, 2005),

317   which has both an anabolic and catabolic component. In the formulation of this Monod-Biomass rate

318   law as implemented in CrunchTope, the thermodynamic term (Gibbs free energy of the reaction) is

319   calculated exclusively using the catabolic pathway. The catabolic pathway for this reaction (in terms

320   of the exchange of one electron) is given below in Equation (4.1), and the form of the Gibbs free

321   energy is this context is given in Equation (4.2) (we take the phosphorylation potential to be 0, and

322   the average stoichiometric number to be 1, see derivation in Jin and Bethke (Jin and Bethke, 2005)

323   for further details).

324
$$\tfrac{1}{8}SO_4^{2-}+\tfrac{1}{8}C_2H_3O_2^-+\tfrac{3}{8}H^+\rightarrow\tfrac{1}{8}H_2S_{(aq)}+\tfrac{1}{4}CO_{2(aq)}+\tfrac{1}{4}H_2O \qquad (4.1)$$

325
$$\Delta G = \mathcal{RT}\ln\left(\frac{[CO_{2(aq)}]^{\frac{1}{4}}[H_2S_{(aq)}]^{\frac{1}{8}}}{\left[SO_4^{2-}\right]^{\frac{1}{8}}[C_2H_3O_2^-]^{\frac{1}{8}}[H^+]^{\frac{3}{8}}}\right) \qquad (4.2)$$

326   Taking this form for the Gibbs free energy of the reaction and substituting it into the thermodynamic

327   term of the reaction rate calculation as implemented in CrunchTope (Steefel et al., 2015) gives

328   Equation (4.3) below describing the rate of microbial sulfate reduction in the Rifle RTM.

329
$$R_{MB} = k_{max}B\frac{[C_2H_3O_2^-]}{[C_2H_3O_2^-]+K_{half[Ace]}}\frac{\left[SO_4^{2-}\right]}{\left[SO_4^{2-}\right]+K_{half\left[SO_4^{2-}\right]}}F_T \qquad (4.3)$$

330   where

331
$$F_T = \left(1 - \frac{[CO_{2(aq)}]^{\frac{1}{4}}[H_2S_{(aq)}]^{\frac{1}{8}}}{\left[SO_4^{2-}\right]^{\frac{1}{8}}[C_2H_3O_2^-]^{\frac{1}{8}}[H^+]^{\frac{3}{8}}}\right) \qquad (4.4)$$

332   R_{MB} is the overall rate of microbial sulfate reduction, k_{max} the rate constant for microbial sulfate

333   reduction, B is the biomass concentration, and $K_{half[X]}$ is a half-saturation constant. The two Monod

334   kinetic factors for the electron donor ($C_2H_3O_2^-$) and the electron acceptor (SO_4^{2-}) are referred to as F_D

335   and F_A respectively (Jin and Bethke, 2003, 2005, 2007). Equation (4.4) illustrates the underlying

336   relationship between pCO$_2$ in the injectate solution and the resulting accumulation of pyrite. As pCO$_2$

337   of in the injectate increases, the F_T term becomes smaller, inhibiting the overall rate of microbial

338   sulfate reduction (Fig. S5). Consequently, biomass growth is also inhibited, and the rate of microbial

339   sulfate reduction is never high enough to produce the concentration of $H_2S_{(aq)}$ required for significant

340   pyrite precipitation. This explains why the model suggests that the gradient of the pyrite volume

341   precipitated with respect to both $C_2H_3O_2^-$ and SO_4^{2-} varies as a function of pCO_2 in the injectate.

342   When pCO_2 is low and both SO_4^{2-} and are large with respect to their half saturation constants

343   (Equation (4.4)), the overall Monod-biomass rate law will approach Bk_{max}.
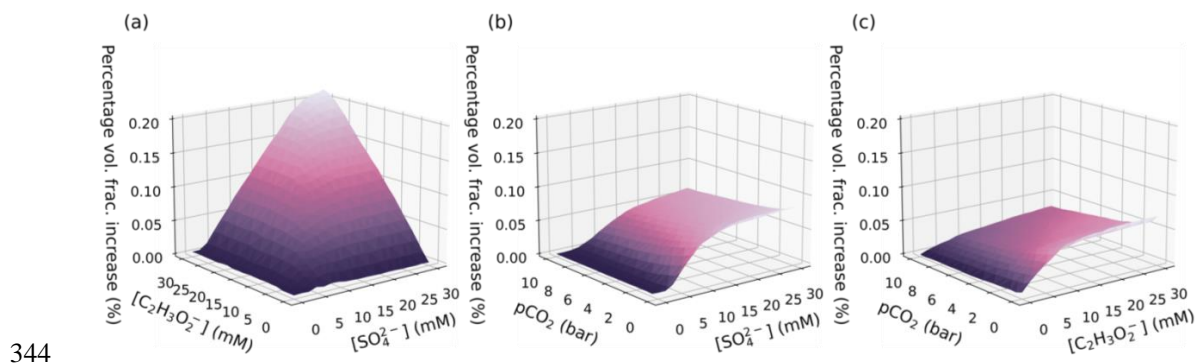
Figure 4: A selection of the GBT model predictions of the percentage volume fraction increase due to pyrite precipitation as a result of varying two parameters simultaneously for selected pairs of variables. Other model parameters are held at the values used in Druhan et al. (2014). The remaining variable-pair plots are provided in Fig. S4.

349   This dependence emerged somewhat unexpectedly from the emulator, as one would not inherently

350   expect a relationship between injectate pCO_2 and SO_4^{2-} reduction rates, yet it agrees with results

351   previously reported by Jin and Kirk (2016, 2018) as well as Paper et al. (2021). These studies related

352   the influence of pCO_2 and pH to the rate of microbial reactions, both *in vitro*, *in situ*, and *in silico*.

353   We suggest that our type of analysis could be used to direct future lab and field work to test

354   hypotheses suggested by the results generated by running the emulator.

355   This analysis also explains some of the features observed in Fig. 4A: the gradients of $C_2H_3O_2^-$ and

356   SO_4^{2-} are coupled in such a way as to indicate that if one is in excess, then the other becomes limiting

357   in the production of $H_2S_{(aq)}$ and hence the precipitation of pyrite. However, the limiting behaviour

358   when both are in excess seems to indicate that given enough SO_4^{2-} and $C_2H_3O_2^-$, pyrite precipitation

359   can continue indefinitely assuming suitably low pCO_2. Given this prediction, it is sensible to check

360   whether, at such high levels of SO_4^{2-} and $C_2H_3O_2^-$ as the model suggests for maximum pyrite

361   precipitation, there is indeed enough Fe(II) available in the system to precipitate pyrite: this is a

362   second potential dependence as mentioned above.

363   Lastly, the model can be interrogated in all 5 dimensions and the amendment fluid composition that

364   corresponds to the largest net pyrite precipitation over the modelled interval can be determined. This

365   amendment composition is shown in Table S1. The total change in volume fraction due to pyrite

366   precipitation predicted by the emulator is 0.143 and the actual RTM modelled precipitation when this

367   boundary condition is used is 0.150. There is a 4.7% absolute error on the net pyrite volume fractions

368   change predicted by the emulator when compared to the actual net pyrite precipitation calculated by

369   the RTM. This error is inherent in statistical learning techniques but can be further mitigated with

370   larger training datasets, in conjunction with different emulator training hyperparameterisations: an

371   area for future improvement to the methodology. These optimised conditions represent an almost

372   four-fold increase in the amount of pyrite precipitated in the original RTM for Old Rifle (Druhan et

373   al., 2014).

4.2   Advantages and drawbacks of the emulation approach

375   In this study, 9416 individual RTM simulations were used to train a GBT regression model to predict

376   a specific model output, in this case net pyrite precipitation. This emulator is a reduced representation

377   of the complex system of equations in the underlying RTM, having a faster computational time but

378   introducing some prediction errors. We now discuss the key advantages and drawbacks of this

379   emulation approach.

4.3   Advantages of the emulation approach

381   9416 RTM runs were used to train the emulator (the data shown in Fig. 2). This number of runs could

382   instead be used to perform a sensitivity analysis in all five variables at a spacing of ~4.8 mM between

383   points by directly interrogating the simulator. What then, is the advantage of the emulation approach,

384   if the same information can be visualised from discreet runs of the original RTM without having to

385   go to the extra effort to train the model, which introduces prediction errors? The key advantages are

386   outlined below.

4.3.1 Advantages over directly interrogating the simulator

388   The first and most obvious advantage is the lack of a need for an explicit interpolation scheme.

389   Correlations generated by directly plotting simulator results in both test cases lead to data points

390   lying on a grid of finite resolution. If intermediate values on this grid were to be determined, an

391   explicit interpolation scheme would have to be applied, which would introduce errors of its own that

392   would then need to be quantified. Furthermore, an improvement in the interpolation scheme would

393   come at the expense of adding one extra point to the grid in each dimension: in the context of Old

394   Rifle this is an extra 9031 data points ($7^5 - 6^5 = 9031$ going from a 5D grid of 6 points in all

395   directions to 7) roughly doubling the dataset size. In contrast, since any number of points can be

396   submitted to the emulator for inference, concerns relating dataset size to sampling resolution are

397   assuaged. Beyond that, the errors in the model fit are already quantified during training.

398   More broadly, to explore the dataspace, emulators are extremely fast compared to simulators. The

399   time for a single query of the emulator is on the order of milliseconds rather than the

400   seconds/minutes/hours for a single forward RTM simulation. This allows the emulator to be used as a

401   tool for efficiently exploring the simulator by rapidly developing intuition for the space itself and

402   how the simulator behaves in different circumstances. Furthermore, emulator models are easy to

403   distribute and share with collaborators. Model weights can be published directly or distributed as

404   standalone files. This means that a well-trained emulator can be made once and then the encoded data

405   shared.

406   Lastly, performing a direct interrogation of the simulator requires choices of parameters and ranges,

407   and results in a grid of points over the region of interest at limited resolution. A similar procedure

408   must be undertaken when creating a dataset to train the emulator, in so far as ranges and parameters

409   of interest must be chosen. However, the dataset can always be further added to in a straightforward

410   manner, further drawing from the random distribution to increase the size of the dataset and thus

411   improve model performance. With both approaches, using Omphalos means that the data generation

412   process can be parallelised and using high-performance computing facilities can reduce the

413   computational expense of interrogating the simulator. This means that all the computational expense

414   is upfront in both cases since the emulator need only be fit once.

415   The advantages we outline make the case for the emulator as a tool to be used in conjunction with the

416   RTM, rather than a replacement for it. The alacrity with which the emulator can be interrogated

417   means that it is an invaluable tool for investigating RTM behaviour in multiple dimensions. Further

418   to this, the ability to evaluate the state of a system after a fixed period of time makes the emulator

419   approach ideally suited for modelling more complex time-series models with time varying boundary

420   conditions: instead of having to run the RTM forward each time the system changes boundary

421   conditions, the emulator can be interrogated for the expected result given the systems current state

422   from the previous regime.

423   Emulation makes sensitivity analysis for RTMs simple and allows us to identify correlations and

424   interactions among parameters that would otherwise be difficult to anticipate, for example the CO_2

425   dependency of microbially mediated reactions (Bethke et al., 2011; Jin and Kirk, 2016, 2018; Paper

426   et al., 2021). This ability to elucidate unexpected but key model dependencies and sensitivities could

427   prove invaluable in helping direct RTM development.

428   **4.3.2 Application to Bayesian optimization**

429   A critical advantage of the technique proposed here is that working emulators are essential to

430   Bayesian optimization. Bayesian optimisation is an approach for finding global maxima and minima

431   in systems whose objective function is expensive to evaluate and does not return the gradients of that

432   function (of which RTMs are an example) (Frazier, 2018). Bayesian optimisation works by applying

433   an acquisition function that calculates the point that will give the most information about the function

434   that requires optimisation. An emulator is then fit using these data points selected by the acquisition

435   function and the emulator is updated with a new point each iteration. In this way, the optimiser

436   balances exploitation of known optima, and exploration of unevaluated regions of the function. Such

437   an approach can find the global maximum with relatively few evaluations of the RTM.

438   This study lays the groundwork for future application of Bayesian optimization to highly

439   dimensioned RTMs, potentially allowing for effective optimization over many different (twenty or

440   more) parameters at once. By demonstrating that broad (but local) fits to the RTM with an emulator

441   are possible, we have demonstrated that a GBT regressor can be used as an emulator informing a

442   Bayesian optimization algorithm in this context. This allows for a constellation of local fits in a

443   highly dimensioned space as the algorithm searches for the global optimum in problems that would

444   otherwise be computationally intractable. Bayesian optimisation could even be applied, with a

445   suitable loss function, to optimise for multiple objectives at once (subject to trade-offs among

446   objectives).

4.4   Disadvantages of the emulation approach

448   This emulation approach relies on the relative computational inexpensiveness of the RTM. In

449   situations where the underlying model is expensive or time-consuming to evaluate, and

450   computational resources are limited, then this modelling approach becomes unfeasible. One way to

451   overcome this limitation is to reduce the resolution of the RTM (as was done in this work), both in

452   time and space, to lower computation time but this comes at the expense of RTM accuracy. In the

453   context of analysing the interaction of underlying modelled processes in an RTM, this loss of

454   resolution may be less of a problem, as we would be primarily concerned with the relationship

455   among parameters and their impact on outputs, rather than their magnitudes. However, this issue of

456   computational expense is primarily allayed by the parallelised generation of data alluded to earlier

457   and only the most expensive RTMs would be intractable for a full emulator fit if this technique was

458   deployed correctly, and even in this extreme case, Bayesian optimisation would still be possible.

459   Additionally, caution is needed when choosing the ranges over which the parameters will be drawn

460   from the uniform random distributions. Key considerations include the number of points being

461   generated relative to the size of the space being covered—a denser cluster of training data will result

462   in a tighter fit, at the expense of range. Conversely, too small of a range and the emulator will not

463   capture key behaviour, or be unable to learn about simulator edge cases, as discussed above with

464   respect to the bioavailable iron in the Old Rifle RTM.

4.5   Choice of learning algorithm

466   Gradient boosted trees outperformed other machine-learning methods that we tested while building

467   the emulators, such as Gaussian process regression. The downsides of GBT include the lack of ability

24

468   to encode smoothness to preclude sharp discontinuities in the concentration-precipitation space or

469   other such prior assumptions. Furthermore, a low root mean squared error over the entire model fit

470   region does not necessarily imply a good fit globally; it may be that there are some regions of good

471   fit and other regions of poor fit which make up an acceptable root mean square error over the whole

472   space.

473   **4.6   The effect of scale on emulator predictions**

474   Our case study relies on the capacity of CrunchTope to predict changes in mineral volume fraction.

475   Therefore, the errors in the predictions, and hence the utility of the approach, ultimately depend on

476   the scale of the system being modelled and thus the sensitivity to what could be very small changes

477   in mineral volume fraction.

478   When analysing the emulator to investigate how different processes in the underlying RTM affect

479   each other, we are primarily considering an issue of whether the emulator can correctly learn the

480   underlying model behaviour. We are also considering whether the emulator can capture the

481   behaviour in the output variables with respect to a changing subset of RTM parameters (some of

482   which we may not have expected at the outset). In this use-case, the emulator is largely concerned

483   with trends and gradients; Figs. Figure 3, Figure 4, S4, S8, and S9 show that this is accurately

484   reported in all case studies. Comparing the case study considered in this paper to the additional case

485   study presented in the Supporting Information we see that they are discretised at different scales (2 m

486   and 1 cm for the deep-sea sediment column and Old Rifle respectively). However, the emulator for

487   each RTM has root mean squared error over the dataset (and hence absolute error in prediction) of

488   the same order of magnitude. This implies that the error in absolute volume precipitated that each

489   model predicts is different. However, the analysis of the trends and interactions emerging from both

490   RTMs is equally valid in both cases.

491   When concerned with the optimisation capabilities of the emulator, the absolute value of the

492   optimised quantity and hence the model scale must be considered. In large-scale systems, such as

493   weathering of the critical zone, the error in the volume fraction change (5.5×10^{-5} for pyrite) is below

494   the resolution of measurement techniques for mineral abundance (e.g. XRD and SEM—(Gu et al.,

495   2020)). However, in smaller-scale systems where the microscale environment becomes increasingly

496   important, these errors in volume fraction become much harder to ignore. For example, in the RTM

497   experiments exploring the effects of scale on simulating mineral dissolution in porous media

498   described by Jung and Navarre-Sitchler (2018), significant errors in changes in predicted volume

499   fraction would propagate into calculated dissolution/precipitation rates, losing sensitivity in the

500   results.

501   **4.7   Extension to multiple outputs**

502   Multiple output regression (the prediction of a vector of outputs, rather than a single label) is in

503   active development for XGBoost and is currently available for other machine learning

504   implementations that we explored, including GPFlow for Gaussian process regression. Given that our

505   approach is currently limited to the prediction of one label-per-emulator trained, the availability of

506   regressors that can predict more than one label 'off the shelf' will greatly improve the utility of

507   reactive transport emulation. The prediction of multiple outputs simultaneously will expand the scope

508   of analysis to investigate the interaction of modelled processes in multiple outputs at once. In the

509   context of optimisation problems, one possible application of the emulator like this could be to

510   maximise mineral precipitation in one region of a system while trying to maximise dissolution in

511   another region.

512   **4.8   Improvements to the model**

513   This proof-of-concept model demonstrates the fitting of an emulator over a relatively small range of

514   environmental parameters. Future work will involve expanding the scope of the emulators both in

515   terms of the number of parameters being varied, but also the range over which they are varied, so the

516   whole behaviour of the underlying model can be captured with more accuracy. There is also scope

517   for adding time dependency to the GBT modelling approach, to predict a time series intermediate

518   RTM states during the evolution of geochemical systems.

519   **4.9   Potential applications**

520   Our emulator approach is flexible; any quantity recorded by an RTM can be used as a target variable,

521   and so the behaviour of any RTM output can be explored in detail to evaluate the model formulation.

522   The behaviour of the system in response to the variation of any parameter under any other set of

523   conditions can be projected out of the model and plotted in a straight-forward manner. This approach

524   can be extended to two or even three dimensions and time series thereof and ultimately the emulator

525   can be interrogated for local maxima and minima to solve optimisation problems. This new approach

526   has potential applications in industry and in environmental remediation where the chemical

527   composition of amendments can be predicted using an underlying reactive transport simulation,

528   provided that that system is well understood.

529   Omphalos also has utility outside of generating datasets for emulation; its automated submission of

530   CrunchTope input files means it can be used to systematically explore sets of input variables in an

531   easy way, simply by editing the Omphalos configuration file.

532   **5   Conclusions**

533   We have presented a new approach for interrogating and understanding multi-component RTMs. By

534   building an emulator of an RTM that captures the multidimensional nature of the underlying model

535   we have created a new tool for performing global sensitivity analyses on RTMs. This allows us to

27

536   investigate behaviour arising from the interaction among the many disparate processes that comprise

537   RTMs. For example, we investigated how the Monod-biomass parameterisation of microbial sulfate

538   reduction interacted with the mechanism of pyrite precipitation. In this example, pyrite precipitation

539   was inhibited when there was an excess of CO_2 in the column because the catabolic pathway was

540   partially dependent on CO_2 concentration. This prevented the growth of sulfate reducing biomass,

541   ultimately curtailing the production of hydrogen sulfide required for pyrite precipitation. This

542   behaviour reproduced results previously reported by Jin and Kirk (2016, 2018), and suggest that our

543   emulation approach has utility in discovering unexpected, but nonetheless real, model behaviours,

544   potentially directing future lab and field work.

545   The approach is flexible; any quantity recorded by an RTM can be used as a target variable, and so

546   the behaviour of any RTM output can be explored in detail to evaluate the model formulation. The

547   behaviour of the system in response to the variation of any parameter under any other set of

548   conditions can be projected out of the model and plot in a straight-forward manner. This approach

549   can be extended to two or even three dimensions and ultimately the emulator can be interrogated for

550   local maxima and minima to solve optimisation problems. This new approach has potential

551   applications in industry and in environmental remediation where the chemical composition of

552   amendments can be predicted using an underlying reactive transport simulation, provided that that

553   system is well understood. The presentation of this optimisation process to Old Rifle (and to ODP

554   Site 1086, see supplementary) represents a proof of concept.

555   **6   Code availability**

556   **6.1   Omphalos**

557   Omphalos is available on GitHub and Zenodo. Please note you must provide your own CrunchTope

558   executable.

559   https://github.com/a-fotherby/Omphalos

560   https://doi.org/10.5281/zenodo.7113298

561   **6.2   GBT Models**

562   Jupyter notebooks for fitting the GBT models and plotting the figures are available on GitHub, and a

563   permanent record is available on Zenodo.

564   https://github.com/a-fotherby/dissertation_xgboost.

565   https://doi.org/10.5281/zenodo.7113323

566   **7   Data availability**

567   The data used is available on GitHub and Zenodo.

568   https://github.com/a-fotherby/GMD_2022

569   https://doi.org/10.5281/zenodo.7113379

570   **8   Supplement**

571   Codebase for Omphalos. Model fitting code. Schematic figures of decision tree and the Old Rifle

572   RTM. Table of predicted optimal values for precipitating pyrite at Old Rifle. Convergence behaviour

573   of the GBT regressors. Additional co-dependency plots for Old Rifle. Figure showing the effect of

574   rate law choice on CO_2 dependency in the Old Rifle RTM. Supplementary Case Study detailing

575   application to a deep-sea sediment column. Description of XGBoost implementation.

576   **9   Author contribution**

577 AF and HJB conceived of the study. AF wrote the codebase and conducted the experiments. AF

578 prepared the manuscript with contributions from all co-authors.

10   Competing interests

580 The authors declare that they have no conflict of interest.

11   Acknowledgements

12   Bibliography

587 Abd, A. S. and Abushaikha, A. S.: Reactive transport in porous media: a review of recent
588 mathematical efforts in modeling geochemical reactions in petroleum subsurface reservoirs, SN
589 Appl. Sci., 3, 401, https://doi.org/10.1007/s42452-021-04396-9, 2021.

590 Anderson, R. T., Vrionis, H. A., Ortiz-Bernad, I., Resch, C. T., Long, P. E., Dayvault, R., Karp, K.,
591 Marutzky, S., Metzler, D. R., Peacock, A., White, D. C., Lowe, M., and Lovley, D. R.: Stimulating
592 the In Situ Activity of Geobacter Species To Remove Uranium from the Groundwater of a Uranium-
593 Contaminated Aquifer, AEM, 69, 5884–5891, https://doi.org/10.1128/AEM.69.10.5884-5891.2003,
594 2003.

595 Arora, B., Dwivedi, D., Faybishenko, B., Wainwright, H. M., and Jana, R. B.: 10. Understanding and
596 Predicting Vadose Zone Processes, in: 10. Understanding and Predicting Vadose Zone Processes, De
597 Gruyter, 303–328, https://doi.org/10.1515/9781501512001-011, 2020.

598 Bain, J. G., Blowes, D. W., Robertson, W. D., and Frind, E. O.: Modelling of sulfide oxidation with
599 reactive transport at a mine drainage site, Journal of Contaminant Hydrology, 41, 23–47,
600 https://doi.org/10.1016/S0169-7722(99)00069-8, 2000.

601 Bargar, J. R., Williams, K. H., Campbell, K. M., Long, P. E., Stubbs, J. E., Suvorova, E. I., Lezama-
602 Pacheco, J. S., Alessi, D. S., Stylo, M., Webb, S. M., Davis, J. A., Giammar, D. E., Blue, L. Y., and
603 Bernier-Latmani, R.: Uranium redox transition pathways in acetate-amended sediments, Proceedings
604 of the National Academy of Sciences, 110, 4506–4511, https://doi.org/10.1073/pnas.1219198110,
605 2013.

606 Bethke, C. M., Sanford, R. A., Kirk, M. F., Jin, Q., and Flynn, T. M.: The thermodynamic ladder in
607 geomicrobiology, American Journal of Science, 311, 183–210, https://doi.org/10.2475/03.2011.01,
608 2011.

609 Beucler, T., Rasp, S., Pritchard, M., and Gentine, P.: Achieving Conservation of Energy in Neural
610 Network Emulators for Climate Modeling, https://doi.org/10.48550/ARXIV.1906.06622, 2019.

611 Bianchi, M., Zheng, L., and Birkholzer, J. T.: Combining multiple lower-fidelity models for
612 emulating complex model responses for CCS environmental risk assessment, International Journal of
613 Greenhouse Gas Control, 46, 248–258, https://doi.org/10.1016/j.ijggc.2016.01.009, 2016.

614 Bone, S. E., Dynes, J. J., Cliff, J., and Bargar, J. R.: Uranium(IV) adsorption by natural organic
615 matter in anoxic sediments, PNAS, 114, 711–716, https://doi.org/10.1073/pnas.1611918114, 2017.

616 van Breukelen, B. M., Griffioen, J., Röling, W. F. M., and van Verseveld, H. W.: Reactive transport
617 modelling of biogeochemical processes and carbon isotope geochemistry inside a landfill leachate
618 plume, Journal of Contaminant Hydrology, 70, 249–269,
619 https://doi.org/10.1016/j.jconhyd.2003.09.003, 2004.

620 Cama, J., Soler, J. M., and Ayora, C.: 15. Acid Water–Rock–Cement Interaction and
621 Multicomponent Reactive Transport Modeling, in: 15. Acid Water–Rock–Cement Interaction and
622 Multicomponent Reactive Transport Modeling, De Gruyter, 459–498,
623 https://doi.org/10.1515/9781501512001-016, 2020.

624 Castruccio, S., McInerney, D. J., Stein, M. L., Liu Crouch, F., Jacob, R. L., and Moyer, E. J.:
625 Statistical Emulation of Climate Model Projections Based on Precomputed GCM Runs*, Journal of
626 Climate, 27, 1829–1844, https://doi.org/10.1175/JCLI-D-13-00099.1, 2014.

627 Chen, T. and He, T.: xgboost: eXtreme Gradient Boosting, 4, 2015.

628 Claesen, M. and De Moor, B.: Hyperparameter Search in Machine Learning,
629 https://doi.org/10.48550/ARXIV.1502.02127, 2015.

630 Doherty, J.: PEST model-independent parameter estimation user manual, Watermark Numerical
631 Computing, Brisbane, Australia, 3338, 3349, 2004.

632 Dolgaleva, I. V., Gorichev, I. G., Izotov, A. D., and Stepanov, V. M.: Modeling of the Effect of pH
633 on the Calcite Dissolution Kinetics, Theor Found Chem Eng, 39, 614–621,
634 https://doi.org/10.1007/s11236-005-0125-1, 2005.

635 Druhan, J. L., Steefel, C. I., Williams, K. H., and DePaolo, D. J.: Calcium isotope fractionation in
636 groundwater: Molecular scale processes influencing field scale behavior, Geochimica et
637 Cosmochimica Acta, 119, 93–116, https://doi.org/10.1016/j.gca.2013.05.022, 2013.

638 Druhan, J. L., Steefel, C. I., Conrad, M. E., and DePaolo, D. J.: A large column analog experiment of
639 stable isotope variations during reactive transport: I. A comprehensive model of sulfur cycling and
640 δ34S fractionation, Geochimica et Cosmochimica Acta, 124, 366–393,
641 https://doi.org/10.1016/j.gca.2013.08.037, 2014.

642 Druhan, J. L., Winnick, M. J., and Thullner, M.: 8. Stable Isotope Fractionation by Transport and
643 Transformation, in: 8. Stable Isotope Fractionation by Transport and Transformation, De Gruyter,
644 239–264, https://doi.org/10.1515/9781501512001-009, 2020.

645 Dullies, F., Lutze, W., Gong, W., and Nuttall, H. E.: Biological reduction of uranium—From the
646 laboratory to the field, Science of The Total Environment, 408, 6260–6271,
647 https://doi.org/10.1016/j.scitotenv.2010.08.018, 2010.

648 Dwivedi, D., Steefel, I. C., Arora, B., and Bisht, G.: Impact of Intra-meander Hyporheic Flow on
649 Nitrogen Cycling, Procedia Earth and Planetary Science, 17, 404–407,
650 https://doi.org/10.1016/j.proeps.2016.12.102, 2017.

651 Dwivedi, D., Steefel, C. I., Arora, B., Newcomer, M., Moulton, J. D., Dafflon, B., Faybishenko, B.,
652 Fox, P., Nico, P., Spycher, N., Carroll, R., and Williams, K. H.: Geochemical Exports to River From
653 the Intrameander Hyporheic Zone Under Transient Hydrologic Conditions: East River Mountainous
654 Watershed, Colorado, Water Resources Research, 54, 8456–8477,
655 https://doi.org/10.1029/2018WR023377, 2018.

656 Finsterle, S., Commer, M., Edmiston, J. K., Jung, Y., Kowalsky, M. B., Pau, G. S. H., Wainwright,
657 H. M., and Zhang, Y.: iTOUGH2: A multiphysics simulation-optimization framework for analyzing
658 subsurface systems, Computers & Geosciences, 108, 8–20,
659 https://doi.org/10.1016/j.cageo.2016.09.005, 2017.

660 Frazier, P. I.: A Tutorial on Bayesian Optimization, arXiv:1807.02811 [cs, math, stat], 2018.

661 Gatel, L., Lauvernet, C., Carluer, N., Weill, S., Tournebize, J., and Paniconi, C.: Global evaluation
662 and sensitivity analysis of a physically based flow and reactive transport model on a laboratory
663 experiment, Environmental Modelling & Software, 113, 73–83,
664 https://doi.org/10.1016/j.envsoft.2018.12.006, 2019.

665 Gaus, I., Azaroual, M., and Czernichowski-Lauriol, I.: Reactive transport modelling of the impact of
666 CO2 injection on the clayey cap rock at Sleipner (North Sea), Chemical Geology, 217, 319–337,
667 https://doi.org/10.1016/j.chemgeo.2004.12.016, 2005.

668 Gharasoo, M., Elsner, M., Van Cappellen, P., and Thullner, M.: Pore-Scale Heterogeneities Improve
669 the Degradation of a Self-Inhibiting Substrate: Insights from Reactive Transport Modeling, Environ.
670 Sci. Technol., 56, 13008–13018, https://doi.org/10.1021/acs.est.2c01433, 2022.

671 Grzeszczuk, R., Terzopoulos, D., and Hinton, G.: NeuroAnimator: fast neural network emulation and
672 control of physics-based models, in: Proceedings of the 25th annual conference on Computer
673 graphics and interactive techniques - SIGGRAPH '98, the 25th annual conference, Not Known, 9–
674 20, https://doi.org/10.1145/280814.280816, 1998.

675 Gu, X., Rempe, D. M., Dietrich, W. E., West, A. J., Lin, T.-C., Jin, L., and Brantley, S. L.: Chemical
676 reactions, porosity, and microfracturing in shale during weathering: The effect of erosion rate,
677 Geochimica et Cosmochimica Acta, 269, 63–100, https://doi.org/10.1016/j.gca.2019.09.044, 2020.

678 Hubbard, S. S., Williams, K. H., Agarwal, D., Banfield, J., Beller, H., Bouskill, N., Brodie, E.,
679 Carroll, R., Dafflon, B., Dwivedi, D., Falco, N., Faybishenko, B., Maxwell, R., Nico, P., Steefel, C.,
680 Steltzer, H., Tokunaga, T., Tran, P. A., Wainwright, H., and Varadharajan, C.: The East River,

681   Colorado, Watershed: A Mountainous Community Testbed for Improving Predictive Understanding
682   of Multiscale Hydrological–Biogeochemical Dynamics, Vadose Zone Journal, 17, 180061,
683   https://doi.org/10.2136/vzj2018.03.0061, 2018.

684   Hubbard, S. S., Agarwal, D., Arora, B., Banfield, J. F., Bouskill, N., Brodie, E., Carroll, R. W. H.,
685   Dwivedi, D., Gilbert, B., Maavara, T., Maxwell, R. M., Newcomer, M. E., Nico, P. S., Sorensen, P.,
686   Steefel, C. I., Steltzer, H., Tokunaga, T. K., Varadharajan, C., Wainwright, H. M., Wan, J., and
687   Williams, K. H.: Key Controls on Water and Nitrogen Exports occurring across Lifezones,
688   Compartments and Interfaces of the Mountainous East River Watershed, CO, 2019, H23B-01, 2019.

689   Jin, Q. and Bethke, C. M.: A New Rate Law Describing Microbial Respiration, Appl Environ
690   Microbiol, 69, 2340–2348, https://doi.org/10.1128/AEM.69.4.2340-2348.2003, 2003.

691   Jin, Q. and Bethke, C. M.: Predicting the rate of microbial respiration in geochemical environments,
692   Geochimica et Cosmochimica Acta, 69, 1133–1143, 2005.

693   Jin, Q. and Bethke, C. M.: The thermodynamics and kinetics of microbial metabolism, American
694   Journal of Science, 307, 643–677, https://doi.org/10.2475/04.2007.01, 2007.

695   Jin, Q. and Kirk, M. F.: Thermodynamic and Kinetic Response of Microbial Reactions to High CO2,
696   Frontiers in Microbiology, 7, 1696, https://doi.org/10.3389/fmicb.2016.01696, 2016.

697   Jin, Q. and Kirk, M. F.: pH as a Primary Control in Environmental Microbiology: 1. Thermodynamic
698   Perspective, Frontiers in Environmental Science, 6, 21, https://doi.org/10.3389/fenvs.2018.00021,
699   2018.

700   Johnson, J. W., Nitao, J. J., and Knauss, K. G.: Reactive transport modelling of CO2 storage in saline
701   aquifers to elucidate fundamental processes, trapping mechanisms and sequestration partitioning,
702   Geological Society, London, Special Publications, 233, 107–128,
703   https://doi.org/10.1144/GSL.SP.2004.233.01.08, 2004.

704   Jung, H. and Navarre-Sitchler, A.: Scale effect on the time dependence of mineral dissolution rates in
705   physically heterogeneous porous media, Geochimica et Cosmochimica Acta, 234, 70–83,
706   https://doi.org/10.1016/j.gca.2018.05.009, 2018.

707   Kashinath, K., Mustafa, M., Albert, A., Wu, J.-L., Jiang, C., Esmaeilzadeh, S., Azizzadenesheli, K.,
708   Wang, R., Chattopadhyay, A., Singh, A., Manepalli, A., Chirila, D., Yu, R., Walters, R., White, B.,
709   Xiao, H., Tchelepi, H. A., Marcus, P., Anandkumar, A., Hassanzadeh, P., and Prabhat: Physics-
710   informed machine learning: case studies for weather and climate modelling, Phil. Trans. R. Soc. A.,
711   379, 20200093, https://doi.org/10.1098/rsta.2020.0093, 2021.

712   Komlos, J., Peacock, A., Kukkadapu, R. K., and Jaffé, P. R.: Long-term dynamics of uranium
713   reduction/reoxidation under low sulfate conditions, Geochimica et Cosmochimica Acta, 72, 3603–
714   3615, https://doi.org/10.1016/j.gca.2008.05.040, 2008.

715   Krasnopolsky, V. M., Fox-Rabinovitz, M. S., and Chalikov, D. V.: New Approach to Calculation of
716   Atmospheric Model Physics: Accurate and Fast Neural Network Emulation of Longwave Radiation
717   in a Climate Model, Monthly Weather Review, 133, 1370–1383,
718   https://doi.org/10.1175/MWR2923.1, 2005.

719 Li, L., Maher, K., Navarre-Sitchler, A., Druhan, J., Meile, C., Lawrence, C., Moore, J., Perdrial, J.,
720 Sullivan, P., Thompson, A., Jin, L., Bolton, E. W., Brantley, S. L., Dietrich, W. E., Mayer, K. U.,
721 Steefel, C. I., Valocchi, A., Zachara, J., Kocar, B., Mcintosh, J., Tutolo, B. M., Kumar, M.,
722 Sonnenthal, E., Bao, C., and Beisman, J.: Expanding the role of reactive transport models in critical
723 zone processes, Earth-Science Reviews, 165, 280–301,
724 https://doi.org/10.1016/j.earscirev.2016.09.001, 2017.

725 Li, Y., Lu, P., and Zhang, G.: An artificial-neural-network-based surrogate modeling workflow for
726 reactive transport modeling, Petroleum Research, 7, 13–20,
727 https://doi.org/10.1016/j.ptlrs.2021.06.002, 2022.

728 Long, P. E., Williams, K. H., Davis, J. A., Fox, P. M., Wilkins, M. J., Yabusaki, S. B., Fang, Y.,
729 Waichler, S. R., Berman, E. S. F., Gupta, M., Chandler, D. P., Murray, C., Peacock, A. D., Giloteaux,
730 L., Handley, K. M., Lovley, D. R., and Banfield, J. F.: Bicarbonate impact on U(VI) bioreduction in a
731 shallow alluvial aquifer, Geochimica et Cosmochimica Acta, 150, 106–124,
732 https://doi.org/10.1016/j.gca.2014.11.013, 2015.

733 Lu, H., Ermakova, D., Wainwright, H. M., Zheng, L., and Tartakovsky, D. M.: DATA-INFORMED
734 EMULATORS FOR MULTI-PHYSICS SIMULATIONS, J Mach Learn Model Comput, 2, 33–54,
735 https://doi.org/10.1615/JMachLearnModelComput.2021038577, 2021.

736 Maavara, T., Siirila-Woodburn, E. R., Maina, F., Maxwell, R. M., Sample, J. E., Chadwick, K. D.,
737 Carroll, R., Newcomer, M. E., Dong, W., Williams, K. H., Steefel, C. I., and Bouskill, N. J.:
738 Modeling geogenic and atmospheric nitrogen through the East River Watershed, Colorado Rocky
739 Mountains, PLOS ONE, 16, e0247907, https://doi.org/10.1371/journal.pone.0247907, 2021a.

740 Maavara, T., Siirila-Woodburn, E. R., Maina, F., Maxwell, R. M., Sample, J. E., Chadwick, K. D.,
741 Carroll, R., Newcomer, M. E., Dong, W., Williams, K. H., Steefel, C. I., and Bouskill, N. J.: Nitrate,
742 ammonium, and DON mass time series output for East River stream, vadose zone and groundwater
743 subwatersheds from HAN-SoMo model, Environmental System Science Data Infrastructure for a
744 Virtual Ecosystem (ESS-DIVE) (United States); Watershed Function SFA,
745 https://doi.org/10.15485/1766811, 2021b.

746 Malaguerra, F., Albrechtsen, H.-J., and Binning, P. J.: Assessment of the contamination of drinking
747 water supply wells by pesticides from surface water resources using a finite element reactive
748 transport model and global sensitivity analysis techniques, Journal of Hydrology, 476, 321–331,
749 https://doi.org/10.1016/j.jhydrol.2012.11.010, 2013.

750 Martinez, B. C., DeJong, J. T., and Ginn, T. R.: Bio-geochemical reactive transport modeling of
751 microbial induced calcite precipitation to predict the treatment of sand in one-dimensional flow,
752 Computers and Geotechnics, 58, 1–13, https://doi.org/10.1016/j.compgeo.2014.01.013, 2014.

753 Molins, S. and Knabner, P.: 2. Multiscale Approaches in Reactive Transport Modeling, in: 2.
754 Multiscale Approaches in Reactive Transport Modeling, De Gruyter, 27–48,
755 https://doi.org/10.1515/9781501512001-003, 2020.

756 Moon, H. S., McGuinness, L., Kukkadapu, R. K., Peacock, A. D., Komlos, J., Kerkhof, L. J., Long,
757 P. E., and Jaffé, P. R.: Microbial reduction of uranium under iron- and sulfate-reducing conditions:
758 Effect of amended goethite on microbial community composition and dynamics, Water Research, 44,
759 4015–4028, https://doi.org/10.1016/j.watres.2010.05.003, 2010.

760   Paper, J. M., Flynn, T. M., Boyanov, M. I., Kemner, K. M., Haller, B. R., Crank, K., Lower, A., Jin,
761   Q., and Kirk, M. F.: Influences of pH and substrate supply on the ratio of iron to sulfate reduction,
762   Geobiology, 19, 405–420, https://doi.org/10.1111/gbi.12444, 2021.

763   Richter, F. M. and DePaolo, D. J.: Numerical models for diagenesis and the Neogene Sr isotopic
764   evolution of seawater from DSDP Site 590B, Earth and Planetary Science Letters, 83, 27–38,
765   https://doi.org/10.1016/0012-821X(87)90048-3, 1987.

766   Rolle, M. and Borgne, T. L.: 5. Mixing and Reactive Fronts in the Subsurface, in: 5. Mixing and
767   Reactive Fronts in the Subsurface, De Gruyter, 111–142, https://doi.org/10.1515/9781501512001-
768   006, 2020.

769   Seigneur, N., Vriens, B., Beckie, R. D., and Mayer, K. U.: Reactive transport modelling to
770   investigate multi-scale waste rock weathering processes, Journal of Contaminant Hydrology, 236,
771   103752, https://doi.org/10.1016/j.jconhyd.2020.103752, 2021.

772   Steefel, C. I., DePaolo, D. J., and Lichtner, P. C.: Reactive transport modeling: An essential tool and
773   a new research approach for the Earth sciences, Earth and Planetary Science Letters, 240, 539–558,
774   https://doi.org/10.1016/j.epsl.2005.09.017, 2005a.

775   Steefel, C. I., DePaolo, D. J., and Lichtner, P. C.: Reactive transport modeling: An essential tool and
776   a new research approach for the Earth sciences, Earth and Planetary Science Letters, 240, 539–558,
777   https://doi.org/10.1016/j.epsl.2005.09.017, 2005b.

778   Steefel, C. I., Appelo, C. A. J., Arora, B., Jacques, D., Kalbacher, T., Kolditz, O., Lagneau, V.,
779   Lichtner, P. C., Mayer, K. U., Meeussen, J. C. L., Molins, S., Moulton, D., Shao, H., Šimůnek, J.,
780   Spycher, N., Yabusaki, S. B., and Yeh, G. T.: Reactive transport codes for subsurface environmental
781   simulation, Comput Geosci, 19, 445–478, https://doi.org/10.1007/s10596-014-9443-x, 2015.

782   Torres, E., Couture, R. M., Shafei, B., Nardi, A., Ayora, C., and Van Cappellen, P.: Reactive
783   transport modeling of early diagenesis in a reservoir lake affected by acid mine drainage: Trace
784   metals, lake overturn, benthic fluxes and remediation, Chemical Geology, 419, 75–91,
785   https://doi.org/10.1016/j.chemgeo.2015.10.023, 2015.

786   Williams, K. H., Long, P. E., Davis, J. A., Wilkins, M. J., N'Guessan, A. L., Steefel, C. I., Yang, L.,
787   Newcomer, D., Spane, F. A., Kerkhof, L. J., McGuinness, L., Dayvault, R., and Lovley, D. R.:
788   Acetate Availability and its Influence on Sustainable Bioremediation of Uranium-Contaminated
789   Groundwater, Geomicrobiology Journal, 28, 519–539,
790   https://doi.org/10.1080/01490451.2010.520074, 2011.

791   Wu, W.-M., Carley, J., Gentry, T., Ginder-Vogel, M. A., Fienen, M., Mehlhorn, T., Yan, H., Caroll,
792   S., Pace, M. N., Nyman, J., Luo, J., Gentile, M. E., Fields, M. W., Hickey, R. F., Gu, B., Watson, D.,
793   Cirpka, O. A., Zhou, J., Fendorf, S., Kitanidis, P. K., Jardine, P. M., and Criddle, C. S.: Pilot-Scale in
794   Situ Bioremediation of Uranium in a Highly Contaminated Aquifer. 2. Reduction of U(VI) and
795   Geochemical Control of U(VI) Bioavailability, Environ. Sci. Technol., 40, 3986–3995,
796   https://doi.org/10.1021/es051960u, 2006.

797   Yoo, A. B., Jette, M. A., and Grondona, M.: SLURM: Simple Linux Utility for Resource
798   Management, in: Job Scheduling Strategies for Parallel Processing, vol. 2862, edited by: Feitelson,

799   D., Rudolph, L., and Schwiegelshohn, U., Springer Berlin Heidelberg, Berlin, Heidelberg, 44–60,
800   https://doi.org/10.1007/10968987_3, 2003.

801